Bulletin of Volcanology (2018) 80: 41
https://doi.org/10.1007/s00445-018-1216-2

RESEARCH ARTICLE

Caldera unrest detected with seawater temperature anomalies at Deception Island, Antarctic Peninsula

M. Berrocoso[1] · G. Prates[1,2,3] · A. Fernández-Ros[1] · L. M. Peci[1] · A. de Gil[1] · B. Rosado[1] · R. Páez[1] · B. Jigena[1]

Received: 3 May 2017 / Accepted: 14 March 2018 / Published online: 24 March 2018

Abstract

Increased thermal activity was detected to coincide with the onset of volcano inflation in the seawater-filled caldera at Deception Island. This thermal activity was manifested in pulses of high water temperature that coincided with ocean tide cycles. The seawater temperature anomalies were detected by a thermometric sensor attached to the tide gauge (bottom pressure sensor). This was installed where the seawater circulation and the locations of known thermal anomalies, fumaroles and thermal springs, together favor the detection of water warmed within the caldera. Detection of the increased thermal activity was also possible because sea ice, which covers the entire caldera during the austral winter months, insulates the water and thus reduces temperature exchange between seawater and atmosphere. In these conditions, the water temperature data has been shown to provide significant information about Deception volcano activity. The detected seawater temperature increase, also observed in soil temperature readings, suggests rapid and near-simultaneous increase in geothermal activity with onset of caldera inflation and an increased number of seismic events observed in the following austral summer.

Keywords Caldera unrest · Seawater temperature anomalies · Deception Island, Antarctic Peninsula

Introduction

There are several examples of submerged calderas throughout the world, located on continental margins (e.g., Nicaragua), arc islands (e.g., Indonesia), and mid-ocean ridges (e.g., Iceland). Most submerged calderas are isolated systems subjected to interactions with the sun's radiation, atmospheric circulation, and rain, snow, or glacier water (Brown et al. 1989; Adams et al. 1990; Hurst et al. 1991; Ohba et al. 1994; Pasternack and Varekamp 1997; Christenson et al. 2010; Delmelle et al. 2015). Calderas forming bays open to the sea (e.g., Thera, Greece) are less common. These open systems are subjected to ocean tides and currents, and present a bigger challenge in terms of monitoring volcanic activity as both temperature and chemical-composition signatures in the water are more easily dissipated, not only to the atmosphere but also out to sea (Sansone et al. 1991; Sansone and Resing 1995).

Many submerged calderas require thorough monitoring due to the volcanic risk to nearby population and infrastructure. The water of submerged calderas can be monitored simply for its color and odor, but it can also be monitored for its temperature, chemical composition, and level (Brown et al. 1989; Adams et al. 1990; Hurst et al. 1991; Ohba et al. 1994; Pasternack and Varekamp 1997; Rouwet et al. 2014). In open systems, these monitoring parameters are more easily diluted and scattered than in isolated systems. Therefore, for water temperature to increase, the heat source input must be higher than the output to the atmosphere in isolated systems and also to the open sea in open systems (Delmelle et al. 2015).

Deception Island has an open-system caldera, Port Foster, its central submerged depression of 7–10 km in diameter

Editorial responsibility: G. Lube

✉ G. Prates
gprates@ualg.pt

[1] Laboratorio de Astronomía, Geodesia y Cartografía, Universidad de Cádiz, Cádiz, Spain

[2] Centro de Estudos Geográficos, IGOT, Universidade de Lisboa, Lisbon, Portugal

[3] Instituto Superior de Engenharia, Universidade do Algarve, Faro, Portugal

opening to the ocean via a single narrow (500 m) and shallow (20 m) channel called Neptune's Bellows. Deception Island itself is 15 km in diameter, and its highest points are Mount Pond at 539 m a.s.l. and Mount Kirkwood at 452 m a.s.l. It is the most prominent active volcanic center in the Bransfield Sea extensional basin between the South Shetland Islands to the northwest and the Antarctic Peninsula to the southeast (Fig. 1a).

The anthropogenic impact at Deception is very low, being almost restricted to austral summer months. Outside of these months, data collected only have an environment input. Being an active volcano on which Antarctic Base Stations are only seasonally operative, every measure of volcanic activity that can be registered year-round is crucial for monitoring. Deception volcano has been monitored based on seismic activity (Carmona et al. 2012), ground deformation (Berrocoso et al. 2012; Prates et al. 2013), and recently on thermal activity (Peci et al. 2014). However, only those sensors with low power consumption, and which are protected from the inhospitable environment, are left operative from late February to early December, when the Base Stations shut and no assistance can be provided to the instruments. Therefore, only the seismic sensor at the Spanish Base Station, the soil temperature at Cerro Caliente, and the tide gauge at Colatinas Point (Fig. 1b) are left operative over this period to monitor the volcanic activity; hence, no ground-deformation measurements or low-energy seismic event hypocenter locations are made from late February to early December.

In June–July 2012, increased thermal activity was detected at Colatinas Point and Cerro Caliente. Pulses of high water temperature at Colatinas Point that coincided with ocean tide cycles were clearer than soil temperature peaks at Cerro Caliente, though no increased seismic activity was reported for June–July 2012 (Carmona et al. 2012; Almendros et al. 2015). However, these thermal anomalies mark the shift from a period of caldera deflation to that of inflation, with an increased number of seismic events observed in the following austral summer. Therefore, we highlight the relevance of monitoring thermal data at submerged calderas, particularly in such inhospitable environments, enhancing the analysis of multi-parameter volcano monitoring datasets.

Regional setting

The South Shetland Islands, apart from Deception Island, are a volcanic arc formed as a consequence of the former Phoenix Plate subduction under the Antarctic plate (González-Ferrán 1991; Livermore et al. 2000; Dietrich et al. 2001; Robertson-Maurice et al. 2003; Taylor et al. 2008; Jin et al. 2009). The regional northeastwards trend of the Antarctic Plate favors roll-back of the subducted Phoenix slab, producing extension in the Bransfield Basin, whose left-lateral component extends back to the left-lateral South Scotia Ridge (Galindo-Zaldívar et al. 2004; Maestro et al. 2007; Solari et al. 2008; Berrocoso et al. 2016). Therefore, the Bransfield Basin has also been considered to be a marginal extensional basin (González-Casado et al. 2000; Fretzdorff et al. 2004), originating from the southwestwards propagation of the South Scotia Ridge that terminates in Deception Island, the southwest limit of the Bransfield Basin (Fig. 1a). These complex geodynamics are manifested in the back-arc volcano-tectonic activity that occurs on Deception Island, whose central submerged depression has been described as a collapse caldera formed after one or more voluminous eruptions (Smellie 2001).

Deception has undergone recent volcanic activity, with confirmed eruptions in 1800, 1812, 1842, 1871, 1912, 1956, 1967, 1969, and 1970 (Torrecillas et al. 2012). Between 1967 and 1970, eruptive process was located around Telefon Bay and Mount Pond (Fig. 1b), which caused the destruction of the Chilean Base in Pendulum Cove, and the collapse of the British Base in Whalers Bay due to a lahar (González-Ferrán and Katsui 1970; González-Ferrán 1995). At the present time, the main surficial indications of volcanic activity on the Island are the occurrence of gas emissions and soil at 100 °C at 107 m a.s.l. on Cerro Caliente; gas emissions and soil at 70 and 100 °C at Whalers Bay and Fumarole Bay, respectively; and thermal springs at Pendulum Cove and Whalers Bay with temperatures of 45 and 65 °C, respectively (García et al. 1997; Ibáñez et al. 2000). Surface water temperatures and chemical composition within the submerged part of the caldera suggest the existence of hydrothermal activity, with higher temperatures, in the north sector of Port Foster. This is close to most of the fumaroles and correlates with volcano-tectonic structures revealed by bathymetric and seismic reflection profiles (Rey et al. 1995; Somoza et al. 2004; Padrón et al. 2015). Recent geomagnetic, gravimetric, and seismic refraction studies further suggest the existence of magma at shallow depths beneath Deception's submerged caldera. Tomography profiles from seismic refraction suggest that Port Foster is underlain by magma detected at about 2-km depth with pronounced low-velocity anomalies beneath Fumarole Bay and also under Mount Pond (Zandomeneghi et al. 2009; Prudencio et al. 2015). Significant seismic activity is also registered on the island. Most of these events are shallow, having low energy, with magnitudes between 1 and 2 (Carmona et al. 2012). Earthquakes of magnitudes 3 and 4 were detected during the seismo-volcanic crisis of 1991–1992 and of 1998–1999. In both crises, the hypocenters were mostly located between Fumarole Bay and Telefon Bay (Ortiz et al. 1997; Ibañez et al. 2000, 2003).

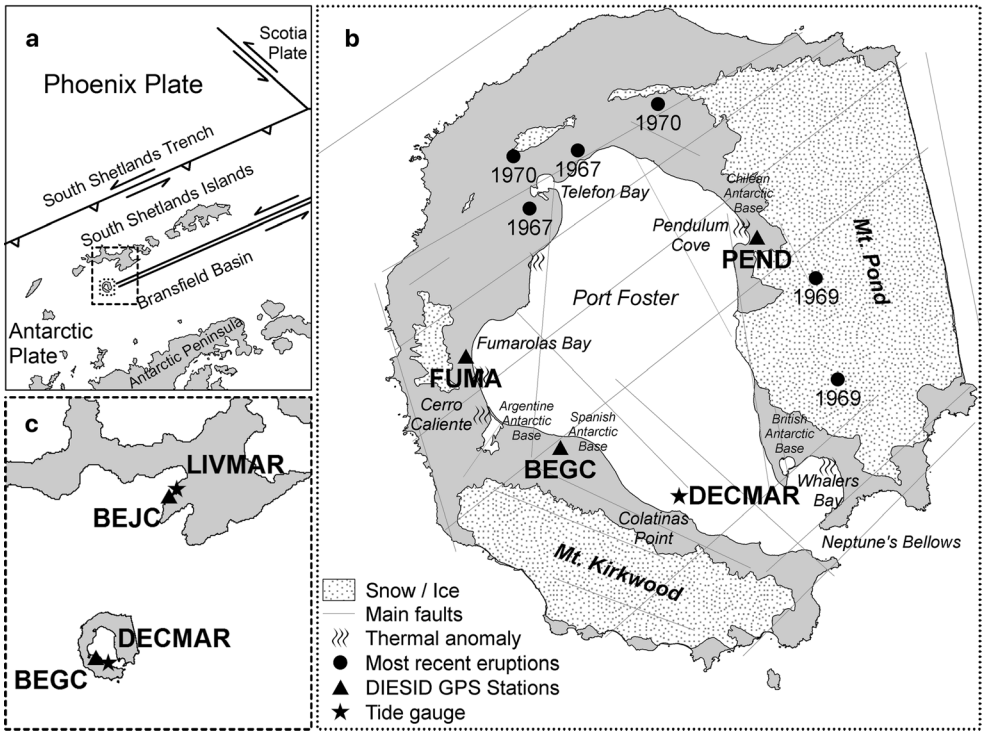

Fig. 1 Deception Island location within the surrounding geodynamic model and location of the thermometric sensors and GNSS-GPS benchmarks. **a** Former Pheonix microplate subducting under the Antarctic plate; Bransfield extensional basin between the South Shetland Islands and the Antarctic Peninsula. **b** Deception Island map showing open vents of the most recent eruptions, relevant sites, main thermal anomalies and location of the ground temperature sensor, CECA, bottom pressure sensor, DECMAR, and GNSS-GPS benchmarks, BEGC, FUMA, and PEND (named DIESID—Deception Island's Spatial Dilatometer and Inclinometer—system including data transmission/reception by WiFi technology and software tools for automatic data processing capability). **c** Location of bottom pressure sensors and reference GNSS-GPS benchmarks on Deception Island (DECMAR, BEGC) and Livingston Island (LIVMAR, BEJC)

Monitoring array and processing methods

In December 2007, two tide gauges (bottom pressure sensors) were installed within the Deception Island submerged caldera at Colatinas Point, DECMAR, and on Livingston Island at Johnsons Dock, LIVMAR. Both tide gauges are linked to geodetic benchmarks, whose coordinates are measured with Global Navigation Satellite Systems–Global Positioning System (GNSS-GPS) (Fig. 1c). On Deception Island, the location was selected because it is as close as possible to one of the few near-shore bedrock outcrops available on the caldera's inner ring, necessary to anchor the weight attached to the bottom pressure sensor, and as near as possible to thermal anomalies, fumaroles, and thermal springs in the north sector of Port Foster. Local ocean tides, mean sea level, and seawater temperature data are registered to monitor volcanic activity, among other parameters. From February 2011, tidal observations at Livingston and Deception became continuous; until that time, they had only been made during the austral summer campaigns. The tidal constituents and the mean sea levels were determined for both locations (Vidal et al. 2011a; Jigena et al. 2015), and the hydrodynamic model for Port Foster was computed (Vidal et al. 2011b).

The bottom pressure sensors were installed to register pressure, temperature, and conductivity. They are located at 5–7- and 2–4-m depth, respectively, in Livingston and Deception, and about 30 m from the coastline where height control benchmarks were fixed into the bedrock. Before and after each data recovery operation, the tide gauges' depth is determined by spirit leveling between the height control benchmark and a second co-located tide gauge closer to the coastline, allowing for correction of the pressure sensor depth in the event of it being displaced by sea ice in the previous winter. Therefore, the observations are linked, providing a continuous mean sea level time series for Livingston and Deception (Jigena et al. 2015).

Seawater temperature and conductivity measurements are carried out to convert the seawater column pressure to tidal height, according to

$$P_h = P_a + \rho\, g\, h$$

where P_h is the hydrostatic pressure registered at the tide gauge, P_a is the local atmospheric pressure (~ 988.27 mb), g is the local gravity acceleration (~ 9.822956 m/s^2), ρ is the seawater density computed from its temperature and

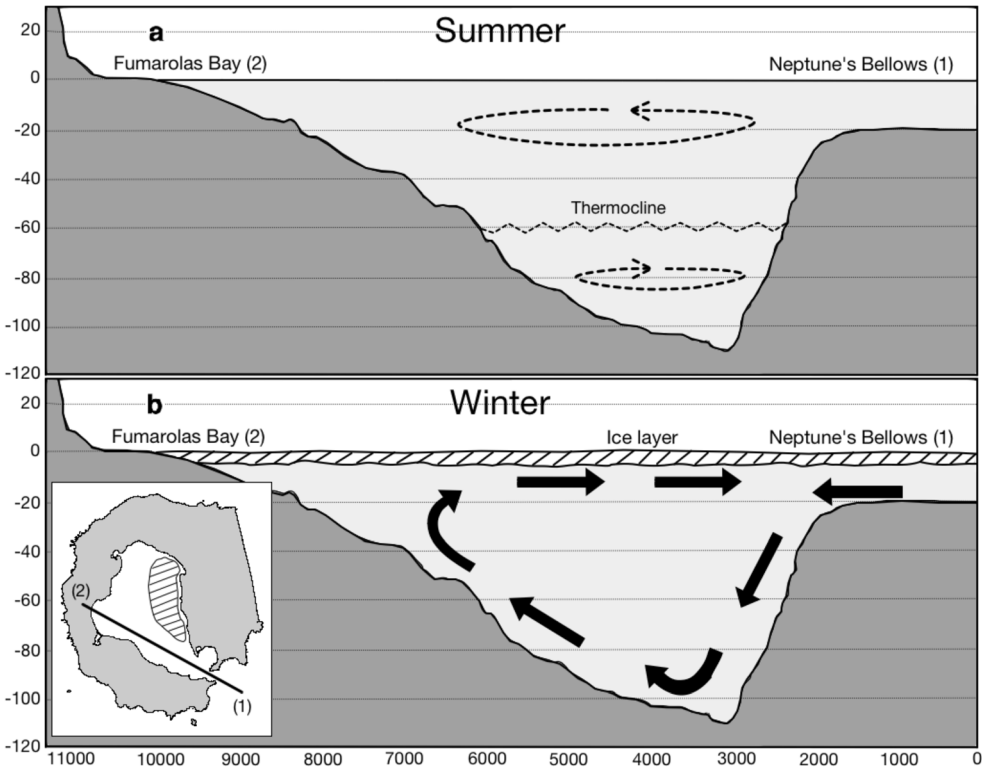

Fig. 2 Port Foster's seasonal hydrodynamic structures. **a** Summer structure with two layers separated by a thermocline at around 60-m depth. **b** Winter structure with a single layer of water at near-freezing temperatures isolated from temperature exchange with the atmosphere by an ice cover

conductivity (Poisson 1980; Millero and Poisson 1981; Millero and Huang 2009; McCleskey et al. 2012), and h is the sea level equivalent height.

Ocean tide constituents and hydrodynamic model

Accounting for Courtier's form number of about 0.8–0.9 in Livingston and Deception, tides were classified as mixed, where 85% of the total tidal energy can be described by M2, S2, K2, N2, K1, O1, P1, and Q1—the eight main tidal constituents. Hence, the tides are predominantly semi-diurnal, where the strongest tidal constituent is M2 with an amplitude of around 0.39 m, followed by K1, O1, and S2 with values of around 0.28 m (Vidal et al. 2011a; Jigena et al. 2015).

Within Deception's inner bay, the poor water exchange rate (1% volume exchange during each tidal cycle) through the narrow opening to the Bransfield Sea and the presence of freshwater from glacier runoff promote Port Foster's water mass temperature and salinity to differ significantly from those of the Bransfield seawater mass (Vidal et al. 2011a). Furthermore, the water circulation within Port Foster is mostly related to ocean tides. Modeled tidal currents are weak inside Port Foster, near 0.10 m/s, with maximum values of 0.76 m/s in the area of the Neptune's Bellows during spring tides, where approximately 90% of the total tidal energy are dissipated (Lenn et al. 2003; Vidal et al. 2011b).

There is a strong seasonal influence on the hydrodynamic circulation regime in Port Foster (Fig. 2). Every summer, atmospheric heating of the sea surface creates a thermocline that produces a two-layer laminar structure. In the upper layer, the circulation is counterclockwise, while in the deeper layer, it is clockwise, caused by coastal-trapped waves traveling at periods of 1–2 days probably triggered by wind gusts (Flexas et al. 2017). As result of shearing processes caused by episodes of high winds as autumn progresses, this configuration changes to a single column of homogeneous water, with temperatures near freezing (~− 1.85 °C) in late winter (Lenn et al. 2003). Also, an inferior mixing potential was found in the eastern side compared to that of the western side of Port Foster, attributed to a westwards radiation of the strong, inwards flowing tidal currents generated at Neptune's Bellows (Flexas et al. 2017).

Seawater temperature data: results

Seasonality is significant, with the warmest water during the summer and high salinity and freezing-point temperatures in the winter (Meredith et al. 2008). At both Deception and Livingston Islands, the seawater temperatures vary year-long between + 2 °C in January and February and − 2 °C from June to October. It is also significant that the data obtained at Deception present greater temperature fluctuations than at Livingston, induced by hydrothermal heating within Port Foster (Fig. 3). In December and January, there are also higher

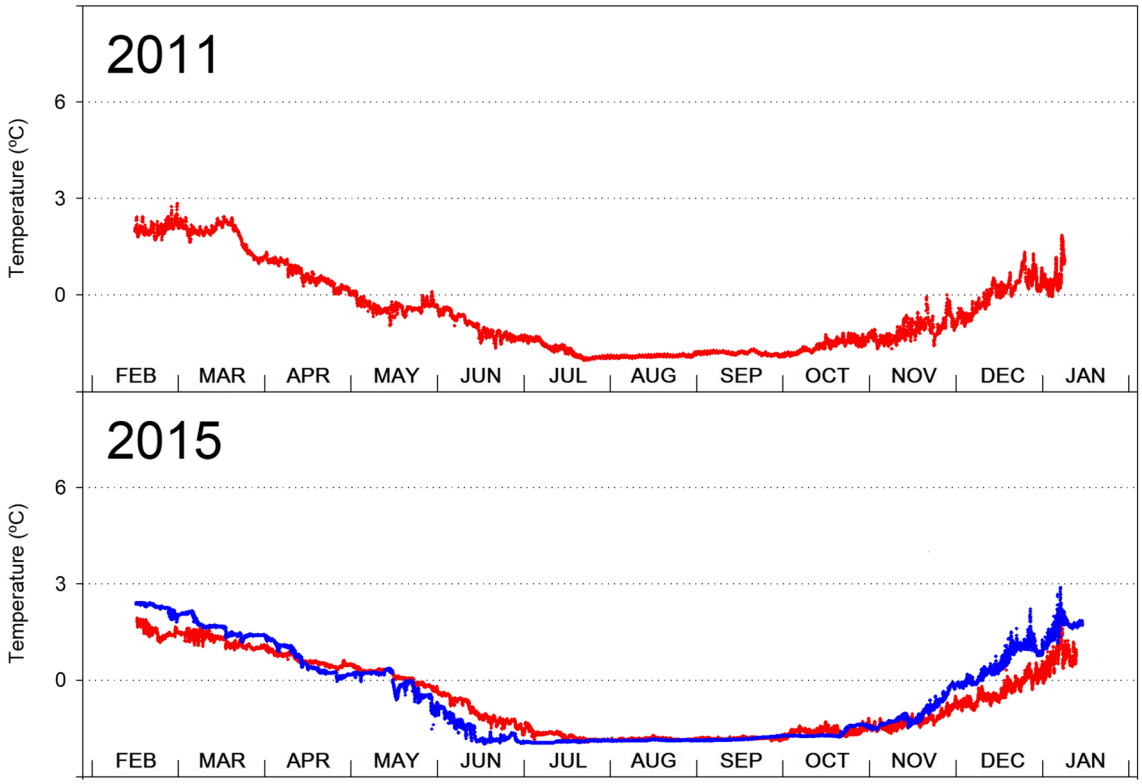

Fig. 3 Seawater temperature comparison by tide gauges deployed in Deception (red), DECMAR, and Livingston (blue), LIVMAR, Islands in 2011 and 2015, depicting similar seasonal trends regionally and inter-annually. The temperature decrease begins later on Deception than on Livingston due to the hydrothermal activity and slow dissipation trough Neptune's Bellows; in the same way, temperature rise begins earlier on Deception than on Livingston, although the seawater temperature in the summer is lower in Deception's inner bay than on Livingston because of the contribution of snow and glacier runoff into a relatively closed system

inputs of freshwater from melting sea ice and glaciers and snow in coastal areas, bringing about significant changes in the salinity (Vidal et al. 2011a).

However, from July 2012 to January 2013, higher temperature fluctuations were registered within Deception's submerged caldera, which was not detected in the preceding or following years (Figs. 3 and 4). These periodic seawater temperature anomalies coincide with the periodic ocean tides, in particular, with the low-tide periodicities of about 12 h, and amplitudes up to and exceeding 10 °C (Fig. 5). The beginning of these temperature anomalies coincides with the lowest seawater temperatures being reached by early July, when the caldera is almost completely covered by sea ice (Smith et al. 2003; Petty et al. 2014), which creates an insulating layer between the seawater and the atmosphere. Towards the summer, the seawater temperature anomaly bursts had not reached the previous 10 °C amplitudes due to the progressive decrease of sea ice within the caldera and consequent temperature dissipation to the atmosphere. By mid-January 2013, the seawater temperature anomalies were no longer detected (Fig. 4).

Higher temperatures were detected after neap tides when tidal currents are weaker and less effective at advecting away the influx of heat from the fumaroles and thermal springs. This allows a higher rise in seawater temperatures in the north sector of Port Foster through thermal conduction. Therefore, the temperature anomaly bursts cause increasing temperatures within the first spring tides, following which the temperature drops as the hot seawater is progressively mixed with cold seawater due to higher tidal currents (Figs. 4 and 5). The low spring tides also favor the warmest uppermost seawater, directly beneath the ice cover, to be closer to the bottom pressure sensor where the seawater temperature is measured.

Therefore, while thermal conduction is responsible for the increase in seawater temperature near fumaroles and thermal springs in the north sector of Port Foster, particularly during neap tides, thermal advection is the main heat transfer process leading to seawater temperature rise near the tide gauge position nearer to the channel leading to the Bransfield Sea in the southeast sector of Port Foster. In fact, from June to October, all temperature rises measured at the tide gauge position correlate with the ocean tides, since the temperature increases from fumarole and thermal spring activity is not sufficient to heat the volume of seawater in Port Foster and reach the tide gauge position by thermal conduction, even in neap tides and in the presence of complete sea ice cover. However, in the north sector of Port Foster, seawater temperature is typically higher (Somoza et al. 2004; Padrón et al. 2015; Flexas et al. 2017) mainly due to thermal conduction.

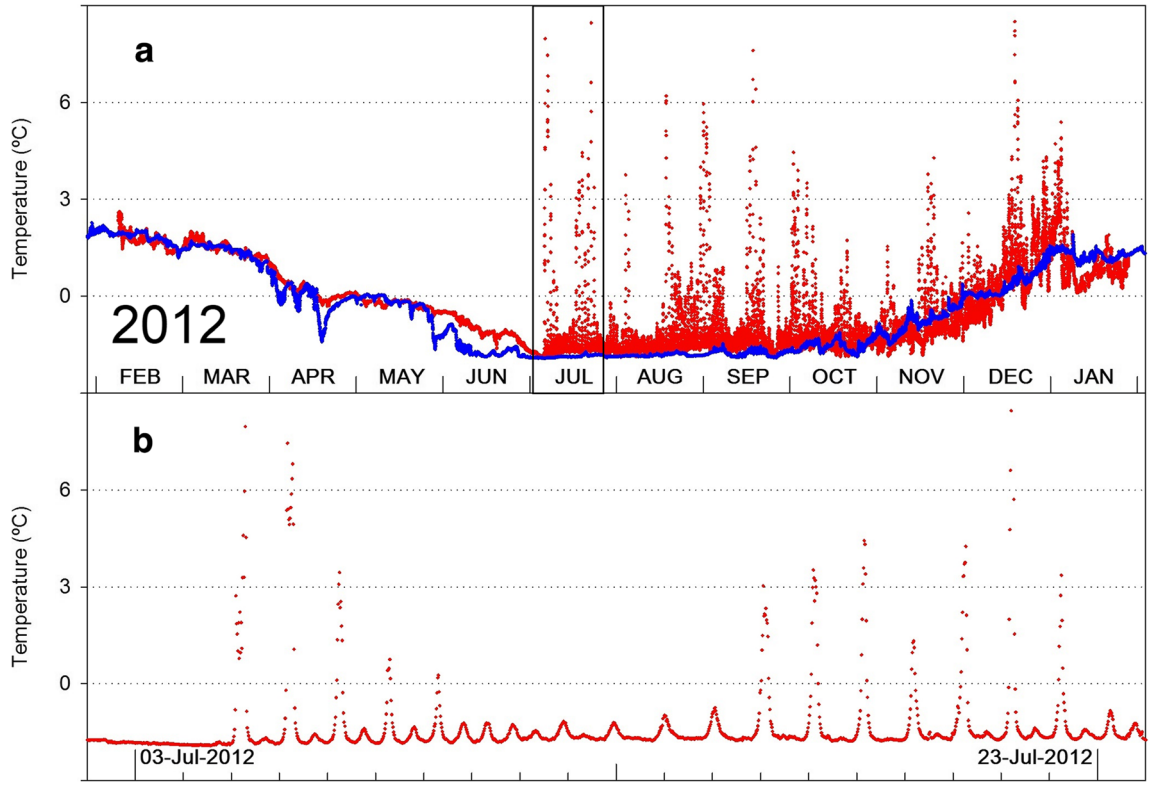

Fig. 4 Seawater temperatures registered at Livingston (blue) and Deception (red) Islands in 2012. **a** The seasonal changes in seawater temperature are similar at Livingston and Deception Islands, with the exception of the temperature anomalies detected at Deception after the lowest seawater temperature is reached. **b** First seawater temperature bursts registered by the thermometric sensor attached to the tide gauge (bottom pressure sensor) with amplitudes reaching over 10 °C

Discussion

Deception volcano activity since 2000 has shown alternating inflation/deflation periods of about 3 years in length (Berrocoso et al. 2012) and corresponding periods of increase/decrease in seismic activity (Carmona et al. 2012). Within its complex geodynamic setting, this periodicity allows us to interpret Deception volcano activity as being controlled by tectonics, where inflation is promoted by extensional stress rather than magma injection. Extensional stress favors increased activity in the submerged caldera hydrothermal system through increased fluid temperature and magma degassing, which brings about ground uplift (Fournier and Chardot 2012). At the shift from compressional to extensional stress, higher fluid temperatures and magma degassing in a permeable medium can be observed as a pore-pressure increase and corresponding higher seismic activity. This is followed by a decrease in both.

The increase in thermal activity in the north sector of Port Foster locally raises the seawater temperature through conduction, which is then advected by tidal currents via Neptune's Bellows through the open passage to the Bransfield Sea. The detection of these seawater temperature anomalies is also favored by the sea ice that insulates the seawater from the atmosphere in the austral winter, hence reducing temperature loss. The water circulation within Port Foster is mostly related to the ocean tides. Towards high tide, Port Foster receives water from the Bransfield Sea, and this is reversed towards low tide. Since the tide gauge is located between the area of thermal activity increase, in the north sector of Port Foster, and Neptune's Bellows, in the southeast sector of Port Foster, it is well located for detecting seawater temperature advection in that area. Only thermal activity in Whalers Bay might not be detected as the seawater may not circulate near the tide gauge.

The detected seawater temperature anomalies coincide with a temporally offset shift in local ground deformation. Ground deformation is determined every austral summer campaign through continuous GNSS-GPS monitoring of three benchmarks (Berrocoso et al. 2008, 2012; Peci et al. 2012; Prates et al. 2013). The normal vector to the triangle they define is computed from the relative positions of these three benchmarks, and the instantaneous strain given by the magnitude of the normal vector is assessed (Berrocoso et al. 2012). Trend shifts in the normal vector magnitude time series, and also in its inclination time series, are monitored between austral summer campaigns, but more importantly, they are monitored in near real time throughout each campaign. During the 2012–2013 campaign, as the sea ice cover disappeared within Port Foster and the seawater temperature anomalies were no longer detected by the thermometric sensor of the tide gauge,

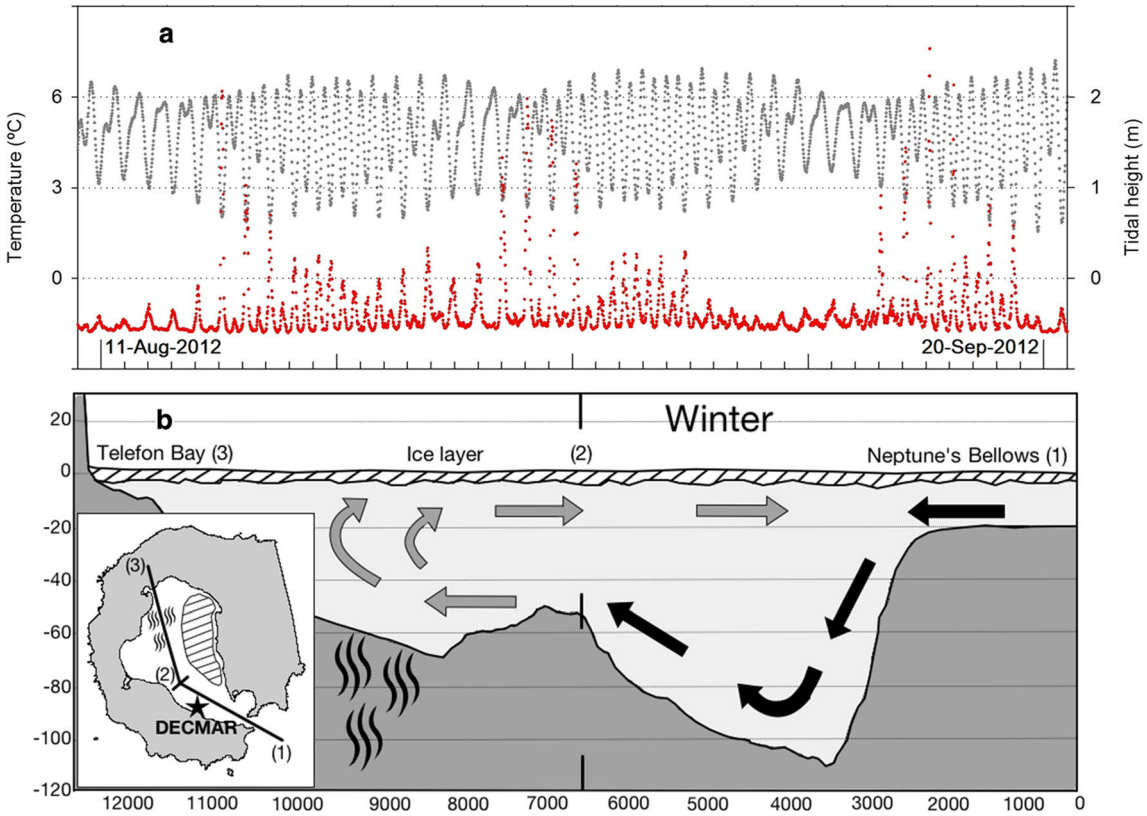

Fig. 5 Seawater temperature and ocean tides registered at Deception Island. **a** Detected seawater temperature anomalies and low tides show a clear correlation, with higher temperatures measured in the low spring tides that follow the neap tides, when lower tidal currents allow the seawater temperature to rise. **b** Water circulation model over one tidal cycle: cold water from the Bransfield Sea passes through Neptune's Bellows towards the inner bay, and warmer water in proximity to hot soil, fumaroles, and thermal springs in the north sector of the inner bay is then cycled towards Neptune's Bellows

the triangle defined by the three benchmarks began an extensional process which was clearly identified by a trend shift in the normal vector magnitude and strain time series (Figs. 6b and 9d). Horizontal and vertical velocities were computed using the inter-annual ground displacement for each GNSS-GPS benchmark, revealing a noticeable geodynamic change from a period of caldera compression and subsidence to extension and uplift (Fig. 6a).

A relative increase in seismicity was also registered in the 2012–2013 austral summer campaign compared to that of the previous summer, both in volcano-tectonic and long-period events (Almendros et al. 2015) (Figs. 7 and 9c), based on a network of four seismic stations deployed every austral summer campaign in the north sector of Port Foster's coastline (Carmona et al. 2012).

Soil temperature peaks in Cerro Caliente (CECA) were also detected in June–July 2012 (Fig. 8a) along with the first seawater temperature bursts. At ground level, the soil temperature is seasonally affected by snow cover; small caves can form at ground level in the snow in which the temperatures are higher due to insulation from the atmosphere, leading to rapid snowmelt within the cave. By wavelet analysis (Mallat 2009), which identifies anomalies in the frequency and amplitude domains of the soil temperature time series, increased thermal activity in the northwest sector of the Port Foster coastline was also detected in late June, July, and August 2012 (Figs. 8a and 9b). In addition, the linear regression over the time series of raw temperature data (Fig. 8a) and its daily averages (Fig. 8b) depicts an increase of about 10 °C from February 2012 to March 2014.

Furthermore, time correlations in mid-July and late August 2012 between two soil and seawater temperature bursts, and later in January 2013 between the increase in seismicity and caldera inflation, were clearly observed through the analysis of this multi-parameter dataset (Fig. 9). Therefore, we consider that the seawater temperature anomalies within Port Foster together with the soil temperature peaks at Cerro Caliente in June–July 2012 marked a shift in the surrounding tectonic stress from compressional to extensional, with consequent increased hydrothermal activity, increased seismicity, and volcano inflation.

Conclusions

From February 2011, continuous tidal data has been acquired for Deception and Livingston Islands. Deception Island is the most prominent active volcano in the Bransfield extensional basin. In

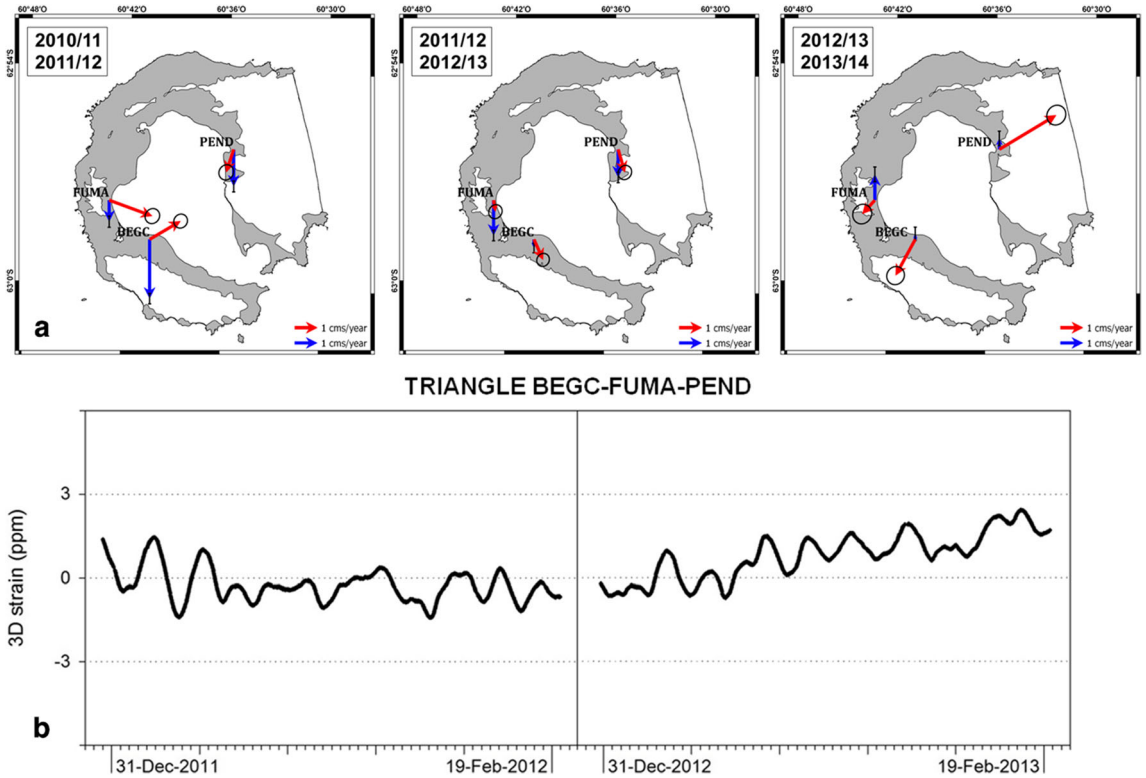

Fig. 6 Deception Island volcano ground deformation from 2010 to 2013 based on three GNSS-GPS benchmarks. **a** Horizontal and vertical velocities of the measured ground displacements of the three benchmarks GNSS-GPS between consecutive austral summer campaigns, without the regional tectonic component, illustrating the shift from compression and subsidence to extension and uplift in this period. **b** Instantaneous strain determined by the ground displacements of the three benchmarks during the austral summer campaigns, in which a clear period of extension is shown in the 2012–2013 austral summer

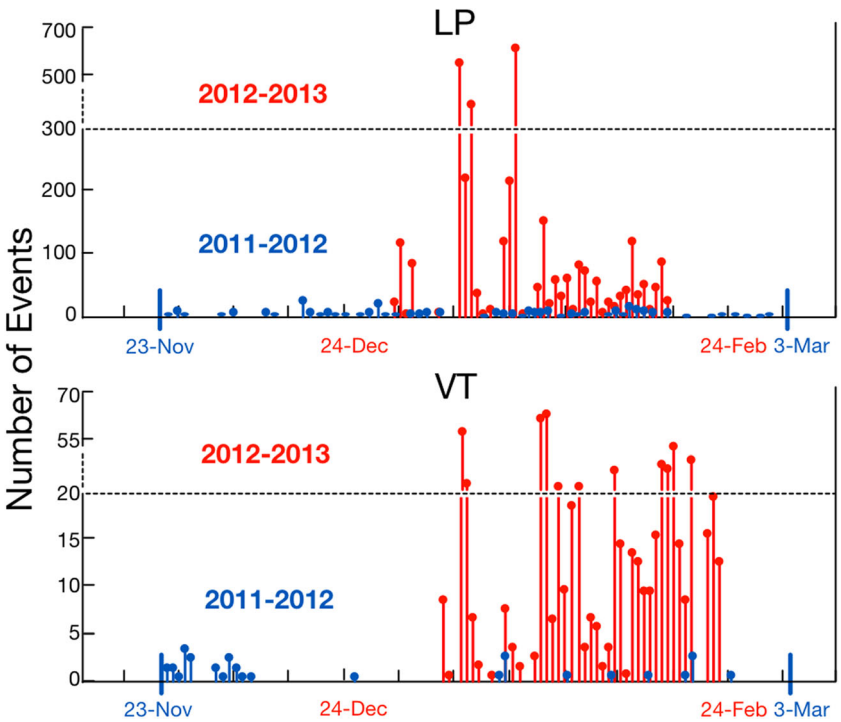

Fig. 7 Seismicity during the austral summer campaigns on Deception Island, indicating the increase of seismicity in the 2012–2013 austral summer. *LP* long period, *VT* volcanotectonic (adapted from Almendros et al. 2015)

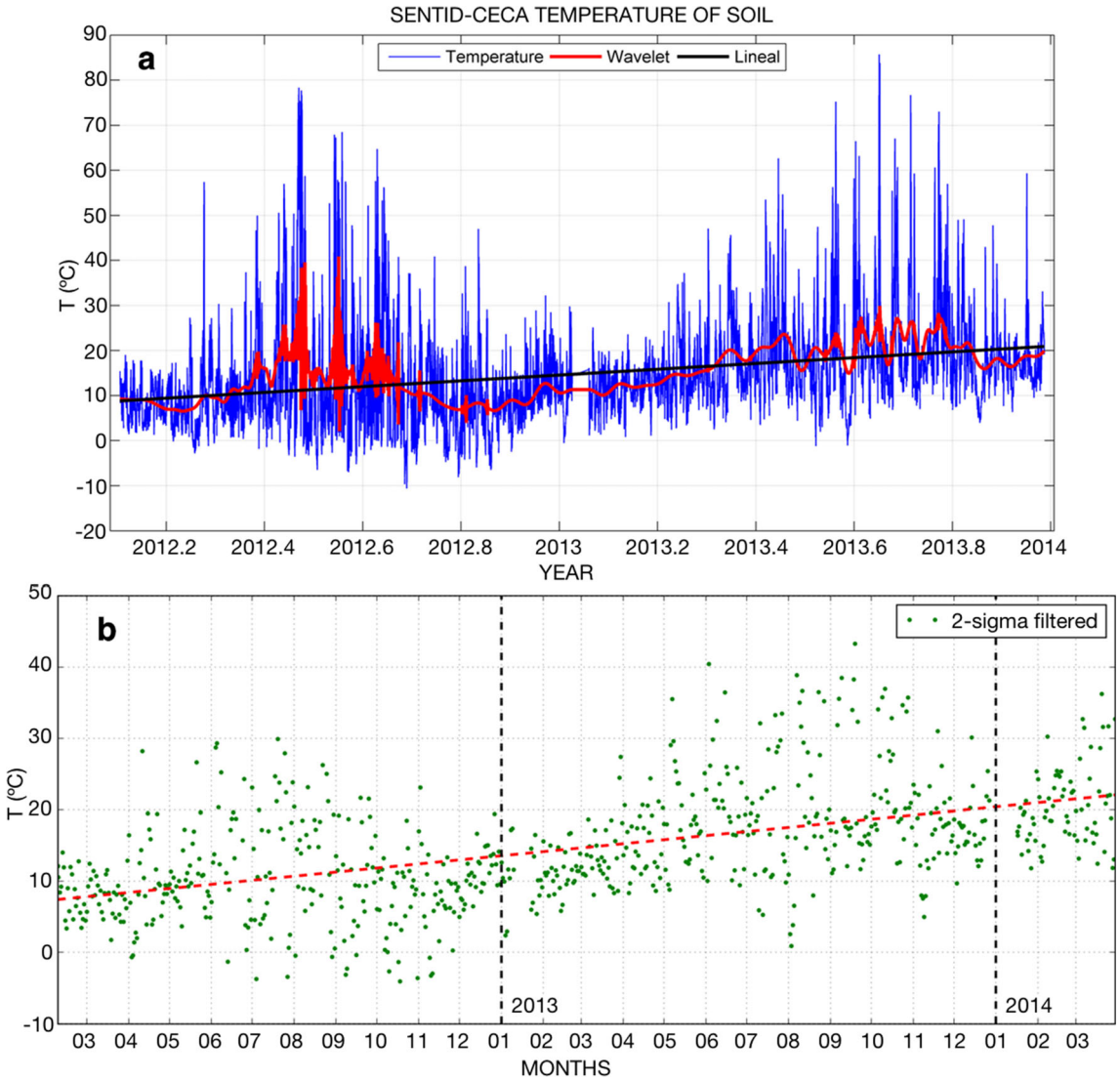

Fig. 8 Soil temperature time series on Cerro Caliente (CECA) for 2012 and 2013. **a** Raw soil temperature (blue), linear regression (black), and wavelet analysis (red), depicting a trend in temperature rise and temperature anomalies with peaks in late June, July, and August of 2012. **b** Daily temperature averages (green) and linear regression (black), depicting the soil temperature increase of about 10 °C over this 2-year time interval

the 2012 austral winter, signatures from seawater temperature anomalies were detected with amplitudes up to and exceeding 10 °C, and periodicities of about 12 h coinciding with the low tides. Soil temperature anomalies in the northwest sector of the Port Foster coastline were also detected in the 2012 austral winter, close to the location of fumaroles and thermal springs. Both suggest an increase in the volcano's hydrothermal system activity. Port Foster sea ice cover in the winter and the tide gauge location favor detection of the seawater temperature anomalies during the austral winter. Therefore, seawater temperature provides valuable information on the dynamic of volcanoes with submerged calderas, such as Deception Island volcano, enhancing the analysis of monitoring datasets.

The increase in volcano activity was confirmed by heightened seismicity between the 2011–2012 and 2012–2013 austral summers. Ground deformation presents a shift from deflation to inflation in 2012, which is shown by the instantaneous strain continuously measured throughout the 2012–2013 austral summer campaign. No ground-deformation measurements are made from late February to early December, and only a single seismic sensor is left operative. Therefore, the seawater temperature anomalies within Port Foster together with the soil temperature in Cerro Caliente filled the data gap between the ground deformation and seismicity campaigns in the austral summers, marking the shift in this volcano dynamics and contributing to acknowledge its volcanic activity as being controlled by tectonics.

Deception Island's horse-shoe shape, with a submerged caldera open to the sea and covered by sea ice in winter, together with the internal tidal currents and the location of

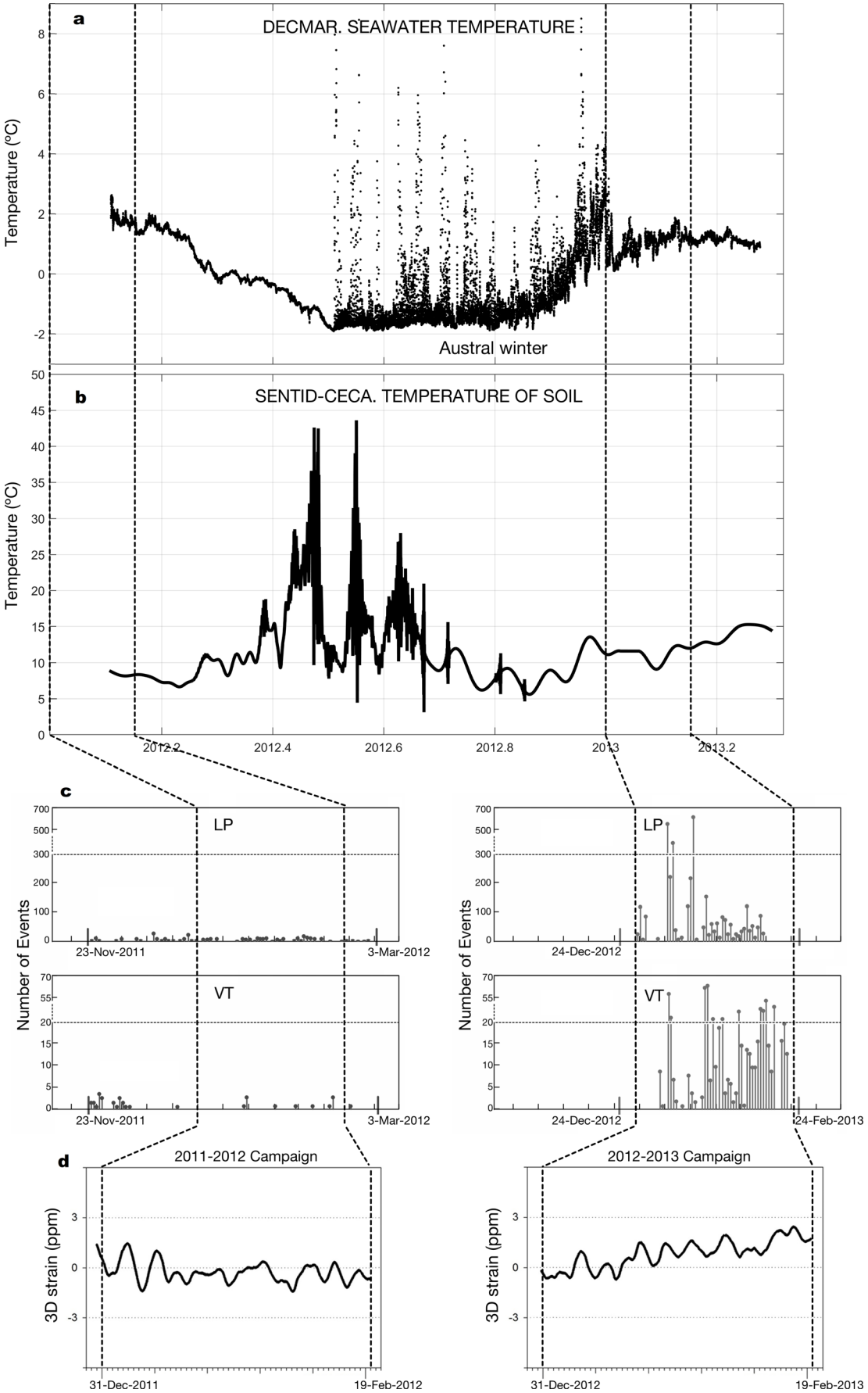
a
DECMAR. SEAWATER TEMPERATURE
Temperature (ºC)
Austral winter
b
SENTID-CECA. TEMPERATURE OF SOIL
Temperature (ºC)
2012.2
2012.4
2012.6
2012.8
2013
2013.2
c
LP
VT
Number of Events
23-Nov-2011
3-Mar-2012
24-Dec-2012
24-Feb-2013
d
2011-2012 Campaign
2012-2013 Campaign
3D strain (ppm)
31-Dec-2011
19-Feb-2012
31-Dec-2012
19-Feb-2013

◀ **Fig. 9** Multi-parameter volcano monitoring dataset for Deception Island. Seawater and soil temperature and ground deformation from GNSS-GPS observed by the Laboratory of Astronomy, Geodesy, and Cartography of the University of Cadiz, and seismicity observed by the Andalusian Institute of Geophysics of the University of Granada (adapted from Almendros et al. 2015). **a** Seawater temperature registered in DECMAR from February 2012 to April 2013. **b** Wavelet analysis of soil temperature in Cerro Caliente from January 2012 to April 2013. **c** Number of LP and VT events recorded in the austral summer campaigns of 2011–2012 and 2012–2013. **d** Normal vector magnitude (strain) in the austral summer campaigns of 2011–2012 and 2012–2013

the bottom pressure sensor, made it possible to identify the seawater temperature changes as the key observable factor in the reactivation of Deception volcano in June–July 2012. Given this setting, the seawater temperature anomalies, together with those of the soil temperature on Cerro Caliente, were precursors to the other analyzed observables—the seismicity and ground-deformation data—registered only in the following austral summer campaign, suggesting rapid and near-simultaneous increase in geothermal activity and the onset of caldera inflation.

Accordingly, at volcanic lakes open to the sea, where assistance to monitoring instrumentation might not be possible for long periods, the thermometric sensor attached to a bottom pressure sensor located where tidal currents advect seawater temperature from volcanic heat sources like thermal anomalies, fumaroles, and thermal springs can effectively acquire relevant data to monitor volcanic activity, also in near-freezing Arctic and Antarctic waters where sea ice cover can provide the necessary isolation from the cold atmosphere and strong winds. As shown, monitoring seawater thermal data at submerged calderas clearly enhances the analysis of monitoring datasets like seismic activity, ground deformation, and soil temperature.

Acknowledgements This geodetic research has been carried out with the support of the Spanish Ministry of Education and Science as part of the National Antarctic Program. The following research projects contributed directly to this work: "Volcano-tectonic activity on Deception Island: geodetic, geophysical investigations and remote sensing on Deception Island and its surroundings (CGL2005-07589-C03-01/ANT)" and "Geodetic and geothermal researches, time serial analysis, and volcanic innovation in Antarctica (South Shetland Islands and Antarctic Peninsula (GEOTINANT) (CTM2009-07251/ANT)." The contributions of both editors and of the reviewers Nicolas Fournier and Magnús T. Gudmundsson are very much appreciated, which greatly helped to improve the manuscript.

References

Adams E, Cosler D, Helfrich K (1990) Evaporation from heated water bodies: predicting combined forced plus free convection. Water Resour Res 26(3):425–435

Almendros J, Carmona E, Jiménez V, Díaz A, Lorenzo F, Berrocoso M, de Gil A, Fernández-Ros A, Rosado B (2015) Report on deception island (Antarctica). In: Venzke E (ed) Bulletin of the Global Volcanism Network, 40:6. Smithsonian Institution

Berrocoso M, Fernández-Ros A, Ramírez ME, Salamanca JM, Torrecillas C, Pérez-Peña A, Páez R, García-García A, Jiménez-Teja Y, García-García F, Soto R, Gárate J, Martín-Davila J, Sánchez-Alzola A, de Gil A, Fernández-Prada JA, Jigena B, (2008) Geodetic research on Deception Island and its environment (South Shetland Islands, Bransfield Sea and Antarctic Peninsula) during Spanish Antarctic Campaigns (1987–2007). In: Capra A, Dietrich R (eds) Geodetic and Geophysical Observations in Antarctica, 97–124

Berrocoso M, Prates G, Fernández-Ros A, García A (2012) Normal vector analysis from GNSS-GPS data applied to deception volcano surface deformation. Geophys J Int 190:1562–1570

Berrocoso M, Fernández-Ros A, Prates G, García A, Kraus S (2016) Geodetic implications on block formation and geodynamic domains in the south Shetland Islands, Antarctic peninsula. Tectonophysics 666:211–219

Brown G, Rymer H, Dowden J, Kapadia P, Stevenson D, Barquero J, Morales L (1989) Energy budget analysis for Poás crater lake: implications for predicting volcanic activity. Nature 339:370–373

Carmona E, Almendros J, Serrano I, Stich D, Ibáñez JM (2012) Results of seismic monitoring surveys of Deception Island volcano, Antarctica, from 1999–2011. Antarct Sci 24:485–499

Christenson BW, Reyes AG, Young R, Moebis A, Sherburn S, Cole-Baker J, Britten K (2010) Cyclic processes and factors leading to phreatic eruption events: insights from the 25 September 2007 eruption through Ruapehu crater Lake, New Zealand. J Volcanol Geotherm Res 19:15–32

Delmelle P, Henley RW, Bernard A (2015) Volcano-related lakes. In: Sigurdsson H, Houghton B, McNutt S, Rymer H, Stix J (eds) The encyclopedia of volcanoes, 2nd edn. Academic Press, Amsterdam, pp 851–864

Dietrich R, Dach R, Engelhardt G, Ihde J, Korth W, Kutterer HJ, Lindner K, Mayer M, Menge F, Miller H, Müller C, Niemeier W, Perlt J, Pohl M, Salbach H, Schenke HW, Schöne T, Seeber G, Veit A, Völksen C (2001) ITRF coordinates and plate velocities from repeated GPS campaigns in Antarctica—an analysis based on different individual solutions. J Geod 74:756–766

Fournier N, Chardot L (2012) Understanding volcano hydrothermal unrest from geodetic observations: insights from numerical modeling and application to White Island volcano, New Zealand. J Geophys Res 117:B11208

Fretzdorff S, Worthington TJ, Haase KM, Hékinian R, Franz L, Keller RA, Stoffers P (2004) Magmatism in the Bransfield Basin: rifting of the south Shetland arc? J Geophys Res 109:B12208

Flexas M, Arias MR, Ojeda MA (2017) Hydrography and dynamics of port Foster, Deception Island, Antarctica. Antarct Sci 29(1):83–93

Galindo-Zaldívar J, Gamboa L, Maldonado A, Nakao S, Bochu Y (2004) Tectonic development of the Bransfield Basin and its prolongation to the south Scotia Ridge, northern Antarctic peninsula. Mar Geol 206(1–4):267–282

García A, Blanco I, Torta JM, Astiz MM, Ibáñez JM, Ortiz R (1997) A search for the volcanomagnetic signal at deception volcano (south Shetland I., Antarctica). Ann Geofis 40(2):319–327

González-Casado JM, Giner-Roles JL, López-Martinez J (2000) Bransfield Basin, Antarctic peninsula: not a normal backarc basin. Geology 28:1043–1046

González-Ferrán O, Katsui Y (1970) Estudio integral del volcanismo cenozoico superior de las Islas Shetland del Sur, Antartica. Serie Cientifica, 1, 123–174, Instituto Antartico Chileno

González-Ferrán O (1991) The Bransfield rift and its active volcanism. In: Thomson, RA, Crame, JA, Thomson, JW (eds) Geological evolution of Antarctica, 505–509

González-Ferrán O (1995) Volcanes de Chile. Instituto Geográfico Militar

Hurst AW, Bibby HM, Scott BJ, McGuinness MJ (1991) The heat source of Ruapehu crater lake; deductions from the energy and mass balances. J Volcanol Geotherm Res 46:1–20

Ibáñez JM, del Pezzo E, Almendros J, la Rocca M, Alguacil G, Ortiz R, García A (2000) Seismovolcanic signals at Deception Island volcano, Antarctica: wavefield analysis and source modeling. J Geophys Res 105:13905–13931

Ibáñez JM, Carmona E, Almendros J, Saccorotti G, del Pezzo E, Abril M, Ortiz R (2003) The 1998–1999 seismic series at Deception Island volcano, Antarctica. J Volcanol Geotherm Res 128(1–3):65–88

Jigena BA, Vidal J, Berrocoso M (2015) Determination of the tide constituents at Livingston and Deception Islands (South Shetland Islands, Antarctica), using annual time series. DYNA 82(191):209-218

Jin YK, Lee J, Hong JK, Nam SH (2009) Is subduction ongoing in the south Shetland trench, Antarctic peninsula?: new constraints from crustal structures of outer trench wall. Geosci J 13(1):59–67

Livermore R, Balanyá JC, Maldonado A, Martínez JM, Rodríguez-Fernández J, Sanz-Galdeano C, Galindo-Zaldívar J, Jabaloy A, Barnolas A, Somoza L, Hernández-Molina J, Suriñach E, Viseras C (2000) Autopsy on a dead spreading center: the Phoenix ridge, drake passage, Antarctica. Geology 28:607–610

Lenn YD, Chereskin TK, Glatts RC (2003) Seasonal to tidal variability in currents, stratification and acoustic backscatter in an Antarctic ecosystem at Deception Island. Deep-Sea Res II 50:1665–1683

Mallat S (2009) A wavelet tour of signal processing—the sparse way. Academic Press, 1–805

Maestro A, Somoza L, Rey J, Martinez-Frias J, Lopez-Martinez J (2007) Active tectonics, fault patterns, and stress field of Deception Island: a response to oblique convergence between the Pacific and Antarctic plates. J S Am Earth Sci 23:256–268

Meredith, M.P., Brandon, A., Wallace, M.I., Clarke, A., Leng, M.J., Renfrew, M.A., van Lipzig, N.P.M., King, J.C., 2008. Variability in the freshwater balance of northern Margarite Bay, Antarctic peninsula: results from $d^{18}O$. Deep-Sea Res II, 55, 309–322

Millero FJ, Poisson A (1981) International one-atmosphere equation of state of seawater. Deep Sea Res A Oceanogr Res Pap 28(6):625–629. https://doi.org/10.1016/0198-0149(81)90122-9

Millero FJ, Huang F (2009) The density of seawater as a function of salinity (5 to 70 g kg^{-1}) and temperature (273.15 to 363.15 K). Ocean Sci 5(2):91–100. https://doi.org/10.5194/os-5-91-2009

McCleskey RB, Nordstrom DK, Ryan JN (2012) Comparison of electrical conductivity calculation methods for natural waters. Limnol Oceanogr Methods 10:952–967. https://doi.org/10.4319/lom.2012.10.952

Ohba T, Hirabayashi J, Nogami K (1994) Water, heat and chloride budgets of the crater lake, Yugama at Kusatsu-Shirane volcano, Japan. Geochem J 28:217–231

Ortiz R, García A, Aparicio A, Blanco I, Felpeto A, Del Rey R, Villegas M, Ibáñez JM, Morales J, Del Pezzo E, Olmedillas JC, Astiz M, Vila J, Ramos M, Viramonte JG, Risso C, Caselli A (1997) Monitoring of the volcanic activity of Deception Island, South Shetland Islands, Antarctica (1986–1995). In: Ricci CA (ed) The Antarctic region: geological evolution and processes, 1071–1076

Padrón E, Hernández PA, Carmona E, Pérez NM, Melían G, Sumino H, Almendros J, Kusakabe M, Wakita H, Padilla GD (2015) Geochemical evidence of different sources of long-period seismic events at deception volcano, south Shetland Islands, Antarctica. Antarct Sci 27(6):557–565

Pasternack GB, Varekamp JC (1997) Volcanic lake systematics I. Physical constraints. J Bull Volcanol 58(7):528–538

Peci, L. M., Berrocoso, M., Páez, R., Fernández-Ros, A., De Gil, A., 2012. IESID: automatic system for monitoring ground deformation on the Deception Island volcano (Antarctica). Comput Geosci, 48, 126–133

Peci LM, Berrocoso M, Fernández-Ros A, García A, Marrero JM, Ortiz R (2014) Embedded ARM system for volcano monitoring in remote areas: application to the active volcano on Deception Island (Antarctica). Sensors 14:672–690

Petty AA, Holland PR, Feltham DL (2014) Sea ice and the ocean mixed layer over the Antarctic shelf seas. Cryosphere 8:761–783

Poisson A (1980) Conductivity/salinity/temperature relationship of diluted and concentrated standard seawater. IEEE J Ocean Eng 5(1):41–50

Prates G, Berrocoso M, Fernández-Ros A, García A (2013) Enhancement of sub-daily positioning solutions for surface deformation monitoring at deception volcano (south Shetland Islands, Antarctica). Bull Volcanol 75:1–10

Prudencio J, De Siena L, Ibáñez JM, Del Pezzo E, García-Yeguas A, Díaz-Moreno A (2015) The 3D attenuation structure of Deception Island (Antarctica). Surv Geophys 36:371–390

Rey J, Somoza L, Martínez-Frías J (1995) Tectonic, volcanic, and hydrothermal event sequence on Deception Island (Antarctica). Geo-Mar Lett 15(1):1–8

Robertson-Maurice SD, Wiens DA, Shore PJ, Vera E, Dorman LMM (2003) Seismicity and tectonics of the south Shetland Islands and Bransfield Strait from a regional broadband seismograph deployment. J Geophys Res 108(B10):2461–2472

Rouwet D, Tassi F, Mora-Amador R, Sandri L, Chiarini V (2014) Past, present and future of volcanic lake monitoring. J Volcanol Geotherm Res 272:78–97

Sansone FJ, Resing JA (1995) The heat source of Ruapehu crater Lake; deductions from the energy and mass balances. J Geophys Res 100(C7):13555–13569

Sansone FJ, Resing JA, Tribble GW, Sedwick PN, Kelly KM, Hon K (1991) Lava-sea water interactions at shallow-water submarine lava flows. Geophys Res Lett 18(9):1731–1734

Smith KL Jr, Baldwin RJ, Glatts RC, Chereskin TK, Ruhl H, Lagun V (2003) Weather, ice, and snow conditions at Deception Island, Antarctica: long time-series photographic monitoring. Deep-Sea Res II 50:1649–1664

Smellie JL (2001) Lithostratigraphy and volcanic evolution of Deception Island, south Shetland Islands. Antarct Sci 13:188–209

Solari MA, Hervé F, Martinod J, le Roux JP, Ramirez LE, Palacios C (2008) Geotectonic evolution of the Bransfield basin, Antarctic peninsula: insights from analogue models. Antarct Sci 20:185–196

Somoza L, Martínez-Frías J, Smellie JL, Rey J, Maestro A (2004) Evidence for hydrothermal venting and sediment volcanism discharged after recent short-lived volcanic eruptions at Deception Island, Bransfield Strait, Antarctica. Mar Geol 203(1–2):119–140

Taylor FW, Bevis MG, Dalziel IWD, Smalley R Jr, Frohlich C, Kendrick E, Foster J, Phillips D, Gudipati K (2008) Kinematics and segmentation of the south Shetland Islands-Bransfield basin system, northern Antarctic peninsula. Geochem Geophys Geosyst 9:Q04035

Torrecillas C, Berrocoso M, Pérez-López R, Torrecillas MD (2012) Determination of volumetric variations and coastal changes due to historical volcanic eruptions using historical maps and remote-sensing at Deception Island (West Antarctica). Geomorphology 136(1):6–14

Vidal J, Berrocoso M, Fernández-Ros A (2011a) Study of tides and sea levels at deception and Livingston islands, Antarctica. Antarct Sci 24(2):193–201

Vidal J, Berrocoso M, Jigena B (2011b) Hydrodynamic modeling of Port Foster, Deception Island (Antarctica). In: Tenreiro-Machado, JA, Baleanu D, Luo ACJ (eds) Nonlinear and complex dynamics: applications in physical, biological, and financial systems, 193–203

Zandomeneghi D, Barclay A, Almendros J, Ibañez JM, Wilcock WSD, Ben-Zvi T (2009) Crustal structure of Deception Island volcano from *P* wave seismic tomography: tectonic and volcanic implications. J Geophys Res 114:B06310